*Article*

# Enhanced Indoor Conversion Efficiency of Dye-Sensitized Solar Cells by Optimizing Ball-Milling Process of TiO$_2$ Paste

Daniel Ursu [1], Cristian Casut [1,2], Daiana Albulescu [1,3], Melinda Vajda [1], Cristina Mosoarca [1] and Marinela Miclau [1,*]

1    National Institute for Research and Development in Electrochemistry and Condensed Matter, Dr. A. Păunescu-Podeanu Street, no. 144, 300569 Timişoara, Romania; danielhoratiu@yahoo.com (D.U.); cristian.casut95@e-uvt.ro (C.C.); daiana.albulescu@student.upt.ro (D.A.); vajda.mellinda@yahoo.ro (M.V.); mosoarca.c@gmail.com (C.M.)
2    Physics Faculty, West University of Timisoara, V. Pârvan Ave., no. 4, 300223 Timişoara, Romania
3    Faculty of Industrial Chemistry and Environmental Engineering, Politehnica University Timisoara, Piata Victoriei Street, no. 1, 300006 Timișoara, Romania
*    Correspondence: marinela.miclau@gmail.com

**Abstract:** The rapid spread of the Internet of Things (IoT) along with the development of innovative low-power electronic devices has also driven the development of indoor photovoltaics. In this paper, we propose a simple and economically feasible solution that can improve the efficiency of dye-sensitized solar cells (DSSCs) under indoor light conditions by ~112%, without requiring a complex TiO$_2$ photoanode architecture or the design of new dyes. The ball milling process of the TiO$_2$ paste was optimized for indoor light conditions for the first time, both in terms of efficiency and production costs, by developing a rapid preparation method that can be used industrially for the application of DSSCs. A simple use of 12 mm diameter balls caused beneficial structural modifications, decreasing the size of the crystallites, and leading to a high OH generation on the TiO$_2$ surface responsible for the improvement of energy conversion efficiency.

**Keywords:** indoor photovoltaics; dye-sensitized solar cell; ball-milling process; TiO$_2$ surface

## 1. Introduction

In recent decades, electronic devices have become indispensable tools for society and modern life due to the rapid development and spread of the Internet of Things (IoT) along with the development of innovative, low-power electronic devices, such as mobile gadgets and sensors [1]. A global estimate shows that there were approximately 11.3 billion connected IoT devices at the end of 2020, and by 2025, there should be more than 27 billion [2]. Given the increasing scale of the IoT, significant maintenance costs for a periodic battery replacement must be taken into consideration [3]. Indoor photovoltaics (IPVs) are a potential energy-supply substitute due to their ability to collect ambient light and convert it into electricity [4]. The narrow emission spectrum of the commonly utilized indoor light sources, for example, light-emitting diodes and fluorescent lamps, establishes that the appropriate band gap of indoor light absorber materials is 1.9 eV [5,6]. Thus, the best efficiency of silicon solar cells (a-Si:H IPV) tested in indoor light conditions has reached up to 21% [7], but for commercial a-Si:H IPV, the efficiency is between 4.4% and 9.2% [8].

Recently, dye-sensitized solar cells (DSSCs) have received a lot of interest in the research and development of next generation solar cells, which are a promising alternative to conventional silicon solar cells due to their sufficient power conversion efficiency and projected cost effectiveness [9–12].

Due to the low incident light intensity (0.1–10 W m$^{-2}$) in indoor environments, the visible spectrum is predominantly 200 lux in home areas, and 300–2000 lux in workspaces and other indoor spaces [13,14].

Until now, most researchers have focused on optimizing the dye in DSSC to improve effective light harvesting for indoor light conditions. Therefore, Liu et al. reported a new porphyrin dye Y1A1 with 19.5% PCE under indoor LED light intensity (350 lux) [15]. Reddy et al. fabricated SK7, another porphyrin dye with 19.72% PCE under a T5 light source (6000 lux) [16]. Wang et al. reported organic anthracene-based dyes (AN1, AN3, AN5, AN7, AN8) with 5.45% PCE for the AN3 dye when integrated in a DSSC module with a 0.16 cm$^2$ cell area under artificial light sources (1000 Lux) [17]. To increase the absorption extinction parameters with 27.76%, 28.74%, and 30.45% under a radiation intensity of 600, 1000, and 2500 lux, Jiang et al. produced Y-shaped sensitizers by integrating quinoxaline or quinoxalinoid moieties [18]. Freitag et al. coupled two sensitizers, D35 and XY1, and utilized a copper complex serving as the redox shuttle. In low fluorescent illumination settings (1000 lux), the PCE was 28.9% [19]. Likewise, Cao et al. combined the Y123/XY1b sensitizers with a Cu electrolyte, and the PCE was 31.8% under 1000 lux fluorescent light intensity [20]. Tanaka et al. combined a low-cost 5T with XY1 dye under artificial fluorescent lighting (1000 lux), and the PCE was 29.2% [21]. Michaels et al. combined a small organic L1 dye with XY1 dye, and the results showed an unprecedented PCE of 34% at 1000 lux, 32.7% at 500 lux, and 31.4% at 200 lux using FL irradiation [22]. Zhang et al. obtained a record efficiency for DSSC (1000 lux) in ambient light with a PCE of 34.5% using MS5/XY1b as dyes and the $[Cu(tmby)_2]^{2+/+}$ redox couple [23].

In addition to the optimization of dyes for indoor conditions presented above, photoanode optimization also plays a key role in improving the performance of DSSCs [24,25], ensuring the transport of photogenerated electrons and active sites for dye adsorption [26,27].

Apart from this, the photoanode made from a nanocrystalline porous $TiO_2$ film electrode plays an essential part since the surface characteristics of the cell, including surface area, roughness, porosity, and film thickness, significantly impact the total conversion efficiency of the cell [28,29]. Therefore, it is necessary to develop a rapid preparation for the $TiO_2$ paste that can be used industrially for the application of DSSCs to increase efficiency and lower production costs. Using the high energy planetary ball mill in the preparation of the $TiO_2$ paste to improve DSSC efficiency compared with untreated $TiO_2$ pastes; (i) leads to decreasing the size of the particles [30], (ii) breaks down the bonds between molecules, and (iii) helps to improve dye adsorption due to the high-force impact kinetic energy on the material, as well as the synchronized alternation of centrifugal forces [31,32].

Until now, most studies have focused on the ball-milling process used for DSSCs tested in outdoor conditions. Optimizing the manufacturing process for the $TiO_2$ paste using ball milling has never been studied, even less for the optimization of the paste for DSSCs used in artificial light conditions, which is much more demanding due to the low intensity of light and its capture by the dye.

Most of the studies using the ball-milling process in the manufacture of the outdoor DSSC paste have not optimized this process in terms of energy consumption and DSSC efficiency. Therefore, Seigo Ito et al. prepared porous electrodes with two different methods to disperse the nanocrystalline $TiO_2$ powder (ball-milling route and mortal-grinding route) using 0.5 mm ceramics balls with 8.27% PCE using N-719 dye [33]. Using the same dye, Niu Huang et al. prepared a viscous $TiO_2$ paste by ball milling, using commercially available P25 powder with ethylene glycol and citric acid for 48 h obtaining an efficiency of 7.36% [34]. A 7.98% efficiency was noted by Chang Kook Hong et al. while preparing green phosphors LaPO4:Ce, Tb, or (Mg, Zn)Al11O19:Eu into $TiO_2$ paste using the Planetary Mono Mill for 10 h at 300 rot/min [35]. Yasuhiro Yamamoto et al. prepared a $TiO_2$ paste using the bead mill method between 1 and 7 h, the optimum dispersion conditions providing an efficiency of 10.1% using the N719 dye. Moreover, increasing the dispersion time under ball milling has caused a decrease in particle size and in transparency of the coated film prepared using the screen printing method [36]. Hadja Fatima Mehnane et al. prepared a Sr doped $TiO_2$ paste using a ball mill for 12 h with 7.88% PCE using the N719 dye [37]. Recently, Huy Hao Nguyen et al. prepared a blue $TiO_2$ paste using the ball-milling method for 20 h for DSSC with 6.18% PCE using the N719 dye [38]. N.A. Abdullah et al. prepared $TiO_2$ nanoparticles

as a paste for DSSC using the ball-milling technique for 8 h with 1.18% PCE immersed in the N719 dye. It is noted that the use of the ball-milling technique leads to an increase in the band gap from 3.30 eV (without milling) to 3.71 eV (8 h milling), and a decrease in the crystallite size [39]. A. Nurlaela et al. prepared $TiO_2$ nanoparticles as paste for DSSC from a microcrystalline powder using the high-energy ball-milling technique (0.5, 1, and 1.5 h of ball-milling time) and made a comparison with untreated $TiO_2$ pastes. They found that the particle size decreases after the milling process, and the efficiency of DSSC increases from 0.0988% (for unmilled $TiO_2$ paste) to 0.1715% (for $TiO_2$ paste milled for 0.5 h) [30].

Therefore, all studies presented above highlight only the effect of the ball-milling process on DSSC efficiency without optimizing this process in terms of energy consumption. The paste-preparation process is carried out over a very long period of time, which requires a high electricity consumption and higher maintenance of the ball mill.

To our knowledge, this is the first time that the $TiO_2$ paste ball-milling process was optimized in order to enhance the conversion efficiency of DSSC under indoor light conditions. Using the N719 photosensitizer, this study aimed to elucidate the ball size effect and ball-milling time for the preparation of the $TiO_2$ paste in terms of energy consumption and DSSC efficiency.

The obtained results revealed that the DSSC obtained from $TiO_2$ paste mortared for 3 h with 12 mm balls had an increase in efficiency of ~38% (21.19% PCE) compared to the paste obtained with 5 mm balls (15.36% PCE) under 1000 lux. At the same time, it was noted that, with the increase in the mortaring time from 3 h to 12 h using 12 mm balls, the increase in DSSC efficiency was only 7.7% (22.7% of PCE) under 1000 lux. This could be seen at $J_{sc}$, which increased by only 7 $\mu$A cm$^{-2}$, and *FF* increased by only ~3.7%, insignificant from the point of view of the production costs of the paste.

## 2. Materials and Methods

To set up the FTO glass substrate (7 $\Omega$/sq from Sigma Aldrich, Merck KGaA, Darmstadt, Germany) for the DSSC preparation, it was washed for 30 min using water, ethanol, and acetone at each stage. This was succeeded by a 30-min UV–Ozone exposure (Ossila B.V., Leiden, The Netherlands). The preparation of the $TiO_2$ paste was conducted in accordance with our prior studies [40,41]. Firstly, 100 $\mu$L glacial acetic acid and 50 $\mu$L of $H_2O$ were mixed, then 300 mg ethyl cellulose was dissolved into 15 mL ethanol, and 2 mL terpineol was added. The paste was ultrasonicated for 30 min and placed in a rotary evaporator to obtain the desired viscosity. The paste obtained was introduced into a high energy planetary ball mill (XQM-0.4A, Tencan, Changsha, China) using zirconium jars and balls with different sizes (5 mm, 8.5 mm, 10 mm, and 12 mm in diameter, and 0.445, 2.02, 3.24, and 5.38 g in weight, respectively) at 90% of the critical speed using different times (3–12 h).

For the photoanode fabrication, a single layer of paste was applied onto the previously cleaned FTO glass substrate, using the doctor blade technique. As a masking material, the same tape was used during the deposition process, ensuring uniform film thickness across all samples. The as-obtained films were calcinated at 500 °C for 60 min with 1 °C/min heating rate to avoid substrate cracking. Finally, the photoelectrodes were immersed in a 40 mM $TiCl_4$ solution for 30 min at 70 °C, and calcined at 450 °C with a heating rate of 1 °C/min for 60 min.

The abbreviation of the photoanodes prepared using different diameter balls and different times is as follows: a mm_b h, where a is the ball diameter, and b is the milling time. The results were compared with the reference photoanode-containing $TiO_2$-NP paste [41], untreated with a high energy planetary ball mill followed by a $TiCl_4$ treatment (referred to as $TiO_2$-NP).

The photoanodes were immersed in a 0.1 mM N719 dye mixture in 100% ethanol for five hours. The photoanodes and platinized counter electrode (CE) ($H_2PtCl_6$ on FTO substrate at 400 °C/30 min in air) were sealed at 134 °C with a Meltonix (1170-60) thick spacer. An electrolyte was injected in the area within the electrodes. It involved a solution

of 0.03 M $I_2$, 0.10 M guanidinium thiocyanate, 0.5 M 4 tert-butylpyridine, 0.6 M 1-butyl-3-methyl-immidazolium iodide, and 3-methoxypropylonitrile (MPN).

The absorbance spectra of the photoanodes were obtained from the diffuse reflectance spectra (DSR) in the wavelength spectrum of 300–800 nm at ambient temperature using a UV/Vis/NIR (Lambda 950 UV-Vis-NIR from Perkin Elmer, Waltham, CT, USA) spectrophotometer with a 150 mm integrating sphere.

The I-V characteristic curves of DSSCs were obtained using a Keithley 2450 SourceMeter inside a homemade measurement case with black paint on every component and a LED lighting source (Lexman, E14, 1.8 W, 250 lm, Ronchin, France) lamp holder integrated at the top with 3.00678 W/m$^2$ at 1005.34 lux using a BTS2048-LV spectroradiometer (Gigahertz Optik GmbH, Munich, Germany); inside the box, the light intensities were calibrated using a Mastech MS6610 light meter [42] (Mastech, London, UK).

The electrochemical impedance spectroscopy (EIS) examination of the DSSCs obtained from paste mixing for 3 h using different balls in a Hi-Energy Planetary Ball Mill under indoor LED illumination (1000 lux) using a different bias potential of DSSCs was conducted with a Autolab potentiostat (unit PGZ 402, Metrohm, Herisau, Switzerland).

A portion of each of the pastes obtained was sintered separately at 500 °C to study the structural properties following the milling process using a high-energy planetary ball mill and different ball sizes. The products' compositions were identified using powder X-ray diffraction (XRD, Malvern Panalytical, Malvern, UK), PW 3040/60 X'Pert PRO with Cu-K$\alpha$ radiation ($\lambda$ = 1.5418 Å), within the range of $2\theta$ = 10–80°, at room temperature. Using the KBr pellet method, FTIR spectra were acquired in the 4000–400 cm$^{-1}$ domain using a JASCO-430 Fourier transform spectrometer (Jasco Co., Tokyo, Japan).

## 3. Results and Discussion

XRD diffraction patterns were used to study the effect of a high energy planetary ball mill using different ball sizes and ball-milling time (3 and 12 h) on the phase structure and the phase composition of $TiO_2$. For the paste prepared at 3 h, a decrease in the intensity of the anatase polymorph (1 0 1) crystal plane with increasing ball size could be noted due to the higher mechanical energy of the zirconia balls. This intensity decreased by approximately 11% for the paste made with 5 mm balls, and 23% for 8.5 mm balls, respectively, compared to $TiO_2$_NP. For the paste made with 10 mm and 12 mm balls, no effect on the intensity of the (1 0 1) crystal plane was observed.

According to Figure 1a, each of the diffraction peaks corresponded to JCPDS No. 00-004-0477 as $TiO_2$ crystallized in anatase form, with a tetragonal crystal structure and a I41/amd space group. In addition to this, no additional phases or impurities were detected.
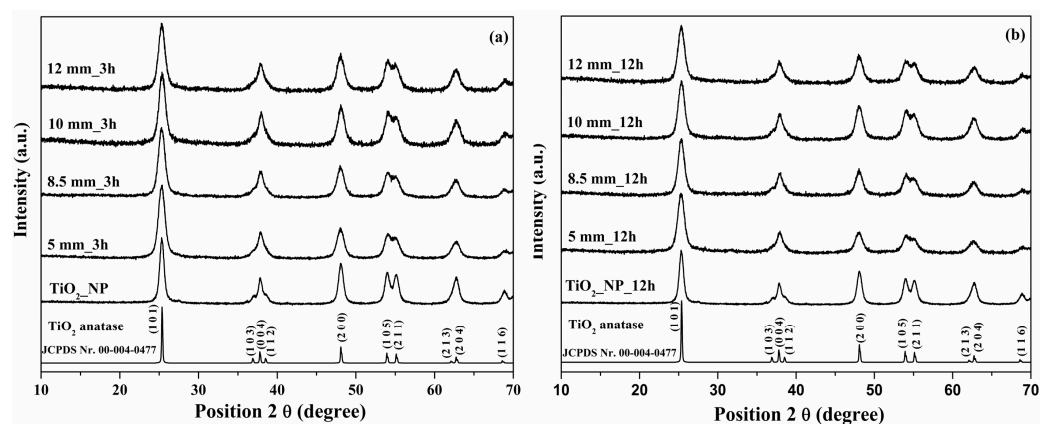


**Figure 1.** X-Ray diffraction patterns for Ti_NP and paste using 5, 8.5, 10, and 12 mm balls at different rotation times (**a**) 3 h and (**b**) 12 h.

For each sample, the dimensions of the crystallite were calculated using the Williamson–Hall (W–H) equation [43]:

$$\beta \cos\theta = \frac{0.9\lambda}{D} + 4\varepsilon \sin\theta \qquad (1)$$

In Equation (1), the notations have the following meaning: β—full width at half maximum (FWHM), θ—diffraction angle of the diffraction peaks, λ—wavelength of X-ray radiation, $D$—effective crystallite size, and ε—lattice strain. The value of $D$, using linear fitting, was given from plotting βcos θ against 4sin θ. In Table 1, the results of the W–H plots show that the crystallite size continuously decreased from 16.3 nm for Ti_NP to 10.3 nm for the paste made with 12 mm balls. The reduced crystallite size correlates strongly with the higher mechanical energy because of the zirconia balls inside the paste.

**Table 1.** Peak (1 0 1) intensity and crystallite size for Ti_NP and paste using 5, 8.5, 10 and 12 mm of balls.

| Sample | Peak (1 0 1) Intensity | | Crystallite Size | |
|---|---|---|---|---|
| | 3 h [%] | 12 h [%] | 3 h [nm] | 12 h [nm] |
| Ti_NP | 100 | 100 | 16.3 | 16.3 |
| 5 mm balls | 89 | 60 | 13.4 | 13.6 |
| 8.5 mm balls | 77 | 50 | 11.7 | 10.4 |
| 10 mm balls | 45 | 50 | 11.3 | 10.3 |
| 12 mm balls | 45 | 45 | 10.3 | 9.5 |

Figure 2 shows the SEM images of the TiO$_2$ photoanode using a high-energy planetary ball mill with 5 mm balls at a 3 h rotation. During the deposition process, the same tape was used for all photoanodes ensuring uniform film thickness across all samples. From the cross-section (Figure 2a), the thickness of the photoanode was 0.85 μm, and from the top section of the obtained photoanodes (Figure 2b), a uniform deposition without cracks could be noted.
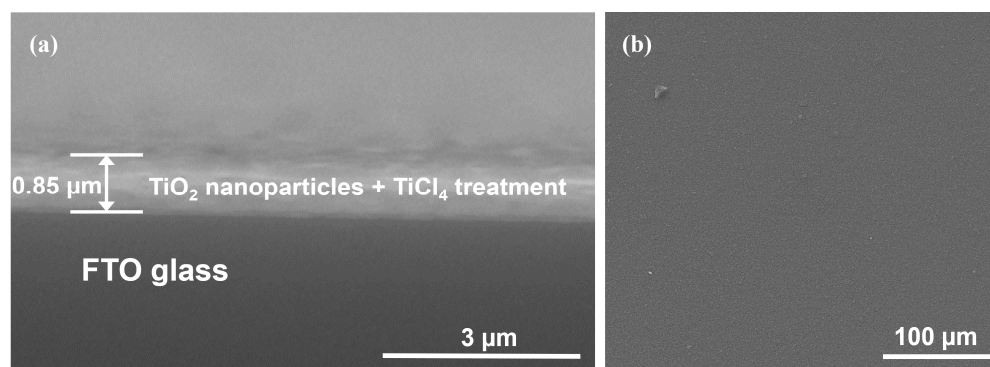


**Figure 2.** SEM images (**a**) cross-section and (**b**) top section of the photoanode obtained using the high energy planetary ball mill with 5 mm of ball sizes and 3 h rotation.

For the 12 h paste (Figure 1b), it could be noted that the intensity of the (1 0 1) crystal plane suddenly dropped by 40% for the paste made with 5 mm balls and continued to decrease to 50% for the paste made with 8.5 mm and 10 mm balls. Even if the grinding time increased from 3 h to 12 h, it could be noted that the intensity of the peak was still 45% for the paste made with 12 mm balls compared to the intensity of the peak for Ti_NP. All of the diffraction peaks were indexed with JCPDS No. 00-004-0477 as TiO$_2$ crystallized in anatase form, and no other phases or impurities were observed. The (1 0 1) peak intensity and crystallite size of the Ti_NP paste using 5 mm balls, 8.5 mm balls, 10 mm balls, and 12 mm balls are shown in Table 1. A similar evolution of the crystalline size determined the value of 9.5 nm for the paste made with 12 mm balls.

Figure 3 shows the optical density spectra of the TiO$_2$ photoanodes using a high-energy planetary ball mill with different ball sizes and different rotation times (3 and 12 h) to prepare the paste. From the optical density spectra of the photoanodes loaded with the N719 dye (Figure 3), it can be noted that the absorption of the dye was improved with an increase in ball size, especially for the paste obtained with the 10 and 12 mm balls. This is due to the fact that decreasing the size of the crystallites confirmed by the XRD analysis allowed the absorption of a much larger amount of dye on the surface of the photoanode, and implicitly led to an increase in the efficiency of DSSC under indoor light conditions [44].
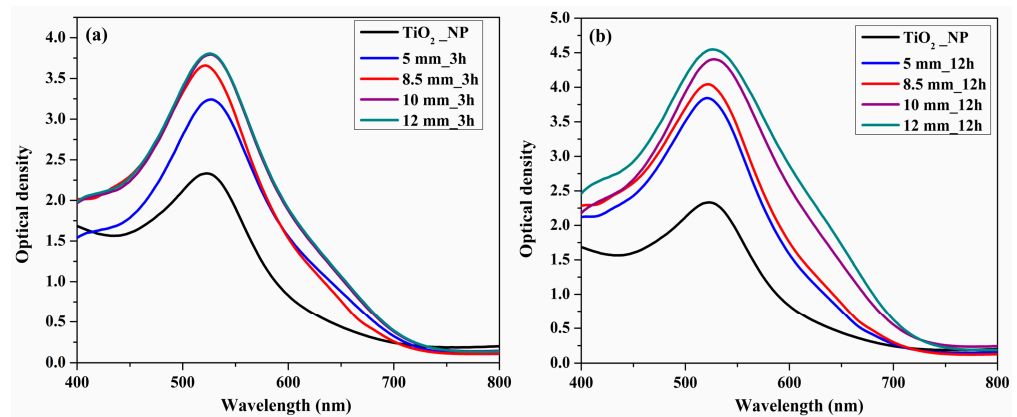


**Figure 3.** Optical density spectra of photoanodes obtained from paste using 5, 8.5, 10, and 12 mm balls at different rotation time (**a**) 3 h and (**b**) 12 h.

The photovoltaic characteristics of the DSSC, obtained from the TiO$_2$ paste using the high-energy planetary ball mill with different ball sizes (5, 8.5, 10, and 12 mm) and rotation times (3 and 12 h) under 1000 lux illumination, are shown in Figure 4. For the DSSC obtained with the paste prepared at 3 h of ball-milling time (Figure 4a), the $J_{SC}$ increased from 112.81 µA cm$^{-2}$ for the paste made with 5 mm balls to 133.83 µA cm$^{-2}$ for the paste made with 8.5 mm balls, to 154.19 µA cm$^{-2}$ for the paste made with 10 mm balls, and to 154.39 µA cm$^{-2}$ for the paste made with 12 mm balls. The results are correlated with the XRD peak (1 0 1) intensity and absorption spectra. For the DSSC obtained with paste using 12 h of ball-milling time (Figure 4b), the $J_{SC}$ increased from 118.88 µA cm$^{-2}$ made with 5 mm balls to 129.39 µA cm$^{-2}$ made with 8.5 mm balls, 160.33 µA cm$^{-2}$ made with 10 mm balls, and 160.91 µA cm$^{-2}$ made with 12 mm balls. For the DSSC using the TiO$_2$-NP paste untreated with the high energy planetary ball mill, a decrease to 81.91 µA cm$^{-2}$ in the $J_{SC}$ value could be noted, due to the high crystallite size compared to the paste treated with the high-energy planetary ball mill, and implicitly an increase of particles size [45].
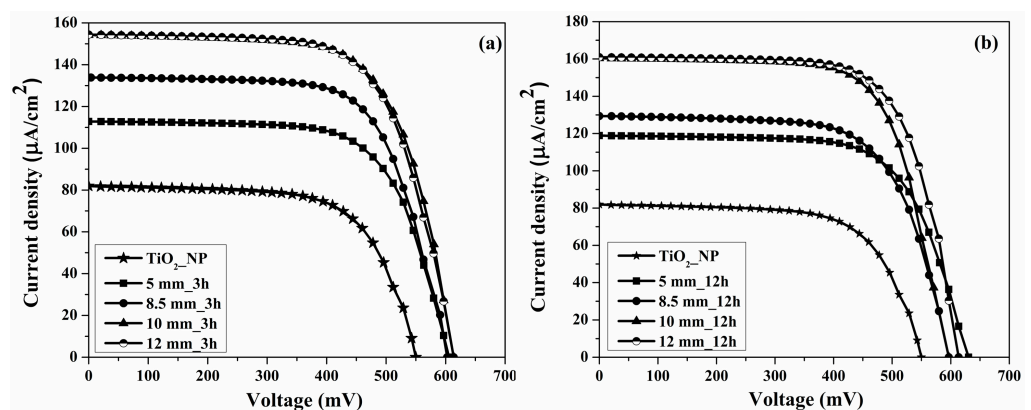


**Figure 4.** J-V measurements of DSSCs for TiO$_2$ paste untreated (TiO$_2$_NP) and obtained from paste milled with 5 mm, 8.5 mm, 10 mm, and 12 mm balls at different rotation time (**a**) 3 h and (**b**) 12 h, under 1000 lux illumination.

According to Table 2, the energy conversion efficiency ($\eta$) was improved with the size of the ball used during the milling process of the TiO$_2$ paste of a photoanode that reliably improved the dye loading capacity. Therefore, for the paste using 3 h of ball-milling time, the energy conversion efficiency has improved from 15.38% with 5 mm balls to 18.22% with 8.5 mm balls, 21.20% with 10 mm balls, and 21.15% with 12 mm balls. The energy conversion efficiency for paste using 12 h of ball milling time was improved from 16.86% with 5 mm balls to 17.21% with 8.5 mm balls, 22.02% with 10 mm balls, and 22.93% with 12 mm balls. For the TiO$_2$-NP paste untreated with high-energy planetary ball mill, the energy conversion efficiency was 9.96%. In terms of production costs (energy consumption and maintenance of high-energy planetary ball mill), the 8.4% increase in energy conversion efficiency does not justify the 12 h used for the ball-milling process compared to 3 h for 12 mm balls.

**Table 2.** Photovoltaic performances of DSSC of untreated TiO$_2$-NP and using different ball sizes (5, 8.5, 10 and 12 mm) and different time (3 and 12 h) to prepare the paste and under 1000 lux illumination conditions [a].

| Nr. Crt. | Time | Materials | $J_{SC}$ [$\mu$A cm$^{-2}$] | $V_{OC}$ [mV] | FF [%] | H [%] |
|---|---|---|---|---|---|---|
| 1 | - | TiO$_2$_NP | 81.91 ± 0.01 | 549.9 ± 0.1 | 66.3 ± 0.1 | 9.96 ± 0.02 |
| 2 | 3 h | 5 mm balls | 112.81 ± 0.01 | 605.6 ± 0.1 | 67.6 ± 0.1 | 15.38 ± 0.04 |
| 3 | | 8.5 mm balls | 133.83 ± 0.01 | 602.7 ± 0.2 | 67.8 ± 0.1 | 18.22 ± 0.03 |
| 4 | | 10 mm balls | 154.19 ± 0.02 | 613.6 ± 0.2 | 67.2 ± 0.1 | 21.20 ± 0.03 |
| 5 | | 12 mm balls | 154.39 ± 0.02 | 613.6 ± 0.2 | 67.0 ± 0.1 | 21.15 ± 0.02 |
| 6 | 12 h | 5 mm balls | 118.88 ± 0.01 | 630.5 ± 0.1 | 67.5 ± 0.1 | 16.85 ± 0.03 |
| 7 | | 8.5 mm balls | 129.39 ± 0.01 | 596.7 ± 0.1 | 66.9 ± 0.1 | 17.21 ± 0.03 |
| 8 | | 10 mm balls | 160.33 ± 0.02 | 596.7 ± 0.2 | 69.1 ± 0.1 | 22.09 ± 0.02 |
| 9 | | 12 mm balls | 160.91 ± 0.02 | 613.6 ± 0.2 | 69.7 ± 0.1 | 22.92 ± 0.02 |

[a] The standard deviation data for each DSSC are obtained based on three cells.

For a deeper understanding of the effect of the ball-milling time and ball sizes on the energy conversion efficiency, the FTIR spectra of the molecular absorption and functional groups of the TiO$_2$ surface were analyzed in correlation with the UV-Vis absorption spectra. All FTIR spectra revealed similar absorption bands with only one exception (Figure 5). Thus, the typical absorption bands at 497–531 cm$^{-1}$ corresponded to the presence of the Ti–O metal oxide bonding [46]; 1631 cm$^{-1}$ was attributed to the bending vibration of –OH, and 3423 cm$^{-1}$ to the stretching mode of the –OH bond [47]. The absorption bands observed at 1380 and 2922 cm$^{-1}$ were also attributed to the C–H bond of the residual organic group of the TiO$_2$ paste after sintering at 500 °C. The intensity of the C–H peak decreased with an increase in ball size in a high-energy planetary ball mill [48,49].
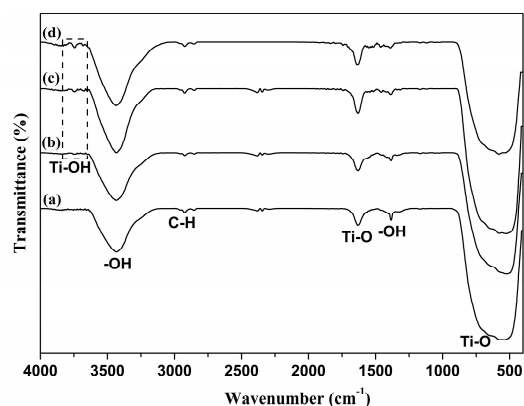


**Figure 5.** FTIR spectra of paste using (a) 5 mm balls, (b) 8.5 mm balls, (c) 10 mm balls, and (d) 12 mm balls at 3 h rotation time.

A special absorption band was detected at 3748 cm$^{-1}$ that may be associated with the hydroxyl group (Ti–OH) of stretching mode of vibration for TiO$_2$ nanoparticles [50]. With ball sizes increasing from 5 to 12 mm, the TiO$_2$ surfaces were highly hydroxylated, improving the presence of the Ti–OH groups. The surface of the Ti–OH groups is amphoteric, and their ionization equilibrium can be written as (Equations (2) and (3)) [51]:

$$\text{Ti–OH}_2^+ \leftrightarrow \text{Ti–OH} + \text{H}^+ \tag{2}$$

$$\text{Ti–OH} \leftrightarrow \text{Ti–O}^- + \text{H}^+ \tag{3}$$

Hirose et al. have shown that OH generation enhances N719 chemisorption on the TiO$_2$ surface and thus leads to an increase in efficiency [52]. In this study, it can be noted that the large generation of OH due to the increase in ball size is in good correlation with the dye-loading capacity of the photoanode is highlighted by the UV-Vis absorption spectra.

In order to better understand the charge dynamics involved in our DSSCs and the impact of TiO$_2$ paste preparation, a study using electrochemical impedance spectroscopy (EIS) was carried out at $V_{OC}$ and under 1000 lux light exposure. The equivalent circuit is shown in the insets of Figure 6, consisting in: $Rs$ intrinsic resistance of the assembled cells, $R_{CE}$ charge transfer resistance at the Pt counter electrode/electrolyte interface [53] and $R_{ct}$ charge transfer resistance at the TiO$_2$ photoelectrode/dye/electrolyte interface [54]. Table 3 summarizes the fitted $Rs$, $R_{CE}$, and $R_{ct}$ values from the equivalent circuit using the Z-view 4 software. The values were in accordance with the photovoltaic parameters of the DSSCs (Table 2).
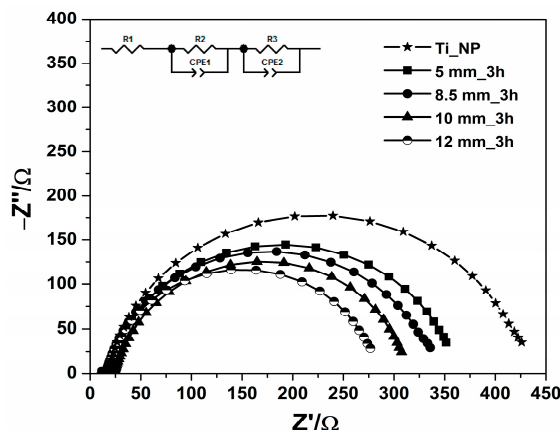


**Figure 6.** Impedance spectra of DSSCs for untreated TiO$_2$ paste (TiO$_2$_NP) and using different ball sizes (5, 8.5, 10, and 12 mm) at 3 h rotation time, under 1000 lux of the illumination intensity. The inset shows the equivalent circuit diagram used to fit the observed impedance spectra.

**Table 3.** EIS parameters obtained from fitting the Nyquist plots of DSSCs for untreated TiO$_2$ paste (TiO$_2$_NP) and using different ball sizes (5, 8.5, 10, and 12 mm) at 3 h rotation time, under 1000 lux illumination intensity.

| DSSC Type | Light Intensity [lux] | $R_S$ [Ω] | $R_{CE}$ [Ω] | $R_{ct}$ [Ω] |
|---|---|---|---|---|
| TiO$_2$_NP | 1000 | 11.6 | 5.6 | 413 |
| 5 mm balls | - | 11.5 | 6.5 | 345 |
| 8.5 mm balls | - | 11.3 | 4.3 | 327 |
| 10 mm balls | - | 11.6 | 7.2 | 292 |
| 12 mm balls | - | 11.5 | 5.2 | 268 |

The intrinsic resistances of the assembled cells ($R_S$) for all DSSCs varied little between 11.3 and 11.6 Ω, having no negative effect on the photovoltaic parameters of the DSSCs. The value of $R_{ct}$ decreased for all cells; for example, by ~35.1% for the DSSC based on the $TiO_2$ paste untreated at high energy planetary ball mill, and by ~22.3% for the DSSC based on the $TiO_2$ paste obtained using a ball size of 12 mm compared to the DSSC based on the $TiO_2$ paste obtained with a ball size of 5 mm, suggesting a decrease in the charge recombination process within the cell, and were reflected in the increase in $J_{SC}$ from the J-V curves. For every DSSC, the $R_{CE}$ values were comparable, indicating that the recombination of charges through the electrolyte and CE was consistent.

## 4. Conclusions

In conclusion, the ball-milling process of the $TiO_2$ paste was optimized for indoor light conditions for the first time, both in terms of efficiency and production costs, by developing a rapid preparation method that can be adopted industrially for the application of DSSCs. Due to the high impact force on the material and the kinetic energy which breaks down the bonds between molecules, a simple use of 12 mm diameter balls caused beneficial structural modifications, decreasing the size of the crystallites, and increasing OH generation on the $TiO_2$ surface for indoor light conditions.

Therefore, the obtained results revealed that the DSSC obtained from the $TiO_2$ paste mortared for 3 h with 12 mm balls highlighted an efficiency increase of ~37.5% (21.15% PCE) compared to the paste obtained with 5 mm balls (15.38% PCE) and 112.3% compared to the untreated paste (9.96% PCE), respectively, at 1000 lux. In terms of production costs, the 8.4% increase in energy conversion efficiency does not justify the 12 h used for the ball-milling process compared to 3 h for 12 mm balls.

Our paper highlights a simple and economically feasible solution that can improve the efficiency of the DSSC under indoor light conditions by ~112.3%, without requiring a complex $TiO_2$ photoanode architecture or the design of new dyes.

**Author Contributions:** Conceptualization, D.U.; methodology, D.U.; validation, M.M.; formal analysis, M.V., C.M., C.C. and D.A.; investigation, D.U.; wring—original draft preparation D.U.; writing—review and editing, M.M, D.U. and M.V.; supervision, M.M. All authors have read and agreed to the published version of the manuscript.

**Institutional Review Board Statement:** Not applicable.

**Informed Consent Statement:** Not applicable.

**Data Availability Statement:** The datasets used and/or analyzed during the current study are available from the corresponding author on reasonable request.

**Conflicts of Interest:** The authors declare no conflicts of interest.

## References

1. Lim, H.-R.; Kim, H.S.; Qazi, R.; Kwon, Y.-T.; Jeong, J.-W.; Yeo, W.-H. Advanced Soft Materials, Sensor Integrations, and Applications of Wearable Flexible Hybrid Electronics in Healthcare, Energy, and Environment. *Adv. Mater.* **2020**, *32*, 1901924. [CrossRef] [PubMed]
2. News, I.B. Number of Connected IoT Devices Growing 9% to 12.3 Billion Globally, Cellular IoT Now Surpassing 2 Billion. Available online: https://iotbusinessnews.com/2021/09/23/13465-number-of-connected-iot-devices-growing-9-to-12-3-billion-globally-cellular-iot-now-surpassing-2-billion/ (accessed on 10 January 2024).
3. Mathews, I.; Kantareddy, S.N.; Buonassisi, T.; Peters, I.M. Technology and Market Perspective for Indoor Photovoltaic Cells. *Joule* **2019**, *3*, 1415–1426. [CrossRef]
4. Pecunia, V.; Occhipinti, L.G.; Hoye, R.L.Z. Emerging Indoor Photovoltaic Technologies for Sustainable Internet of Things. *Adv. Energy Mater.* **2021**, *11*, 2100698. [CrossRef]
5. Wu, M.-J.; Kuo, C.-C.; Jhuang, L.-S.; Chen, P.-H.; Lai, Y.-F.; Chen, F.-C. Bandgap Engineering Enhances the Performance of Mixed-Cation Perovskite Materials for Indoor Photovoltaic Applications. *Adv. Energy Mater.* **2019**, *9*, 1901863. [CrossRef]

6.  Ann, M.H.; Kim, J.; Kim, M.; Alosaimi, G.; Kim, D.; Ha, N.Y.; Seidel, J.; Park, N.; Yun, J.S.; Kim, J.H. Device design rules and operation principles of high-power perovskite solar cells for indoor applications. *Nano Energy* **2020**, *68*, 104321. [CrossRef]
7.  Reich, N.H.; van Sark, W.G.J.H.M.; Turkenburg, W.C. Charge yield potential of indoor-operated solar cells incorporated into Product Integrated Photovoltaic (PIPV). *Renew. Energy* **2011**, *36*, 642–647. [CrossRef]
8.  De Rossi, F.; Pontecorvo, T.; Brown, T.M. Characterization of photovoltaic devices for indoor light harvesting and customization of flexible dye solar cells to deliver superior efficiency under artificial lighting. *Appl. Energy* **2015**, *156*, 413–422. [CrossRef]
9.  Vajda, M.; Ursu, D.; Duteanu, N.; Miclau, M. Low lying valence band edge materials based on copper oxide for tandem dye-sensitized solar cells. *Mater. Lett.* **2020**, *275*, 128151. [CrossRef]
10. Vajda, M.; Ursu, D.; Mosoarca, C.; Duteanu, N.; Miclau, M. Experimental investigation of hydrogen insertion in copper oxide on photovoltaic performance of p-type dye-sensitized solar cell. *Int. J. Energy Res.* **2021**, *45*, 5309–5317. [CrossRef]
11. Miclau, M.; Dabici, A.; Vajda, M.; Ursu, D. CrOOH as high-performance surface passivation material for dye-sensitized solar cell. *Mater. Lett.* **2018**, *216*, 119–122. [CrossRef]
12. Ursu, D.; Banică, R.; Vajda, M.; Baneasa, C.B.; Miclau, M. Investigation of silver nanowires in $Zn_2SnO_4$ spheres for enhanced dye-sensitized solar cells performance. *J. Alloys Compd.* **2022**, *902*, 163890. [CrossRef]
13. Hou, B.; Kim, B.-S.; Lee, H.K.H.; Cho, Y.; Giraud, P.; Liu, M.; Zhang, J.; Davies, M.L.; Durrant, J.R.; Tsoi, W.C.; et al. Multiphoton Absorption Stimulated Metal Chalcogenide Quantum Dot Solar Cells under Ambient and Concentrated Irradiance. *Adv. Funct. Mater.* **2020**, *30*, 2004563. [CrossRef]
14. Lee, H.K.H.; Li, Z.; Durrant, J.R.; Tsoi, W.C. Is organic photovoltaics promising for indoor applications? *Appl. Phys. Lett.* **2016**, *108*, 253301. [CrossRef]
15. Liu, Y.-C.; Chou, H.-H.; Ho, F.-Y.; Wei, H.-J.; Wei, T.-C.; Yeh, C.-Y. A feasible scalable porphyrin dye for dye-sensitized solar cells under one sun and dim light environments. *J. Mater. Chem. A* **2016**, *4*, 11878–11887. [CrossRef]
16. Reddy, K.S.K.; Liu, Y.-C.; Chou, H.-H.; Kala, K.; Wei, T.-C.; Yeh, C.-Y. Synthesis and Characterization of Novel β-Bis(N,N-diarylamino)-Substituted Porphyrin for Dye-Sensitized Solar Cells under 1 sun and Dim Light Conditions. *ACS Appl. Mater. Interfaces* **2018**, *10*, 39970–39982. [CrossRef] [PubMed]
17. Wang, C.-L.; Lin, P.-T.; Wang, Y.-F.; Chang, C.-W.; Lin, B.-Z.; Kuo, H.-H.; Hsu, C.-W.; Tu, S.-H.; Lin, C.-Y. Cost-Effective Anthryl Dyes for Dye-Sensitized Cells under One Sun and Dim Light. *J. Phys. Chem. C* **2015**, *119*, 24282–24289. [CrossRef]
18. Jiang, M.L.; Wen, J.-J.; Chen, Z.-M.; Tsai, W.-H.; Lin, T.-C.; Chow, T.J.; Chang, Y.J. High-Performance Organic Dyes with Electron-Deficient Quinoxalinoid Heterocycles for Dye-Sensitized Solar Cells under One Sun and Indoor Light. *ChemSusChem* **2019**, *12*, 3654–3665. [CrossRef] [PubMed]
19. Freitag, M.; Teuscher, J.; Saygili, Y.; Zhang, X.; Giordano, F.; Liska, P.; Hua, J.; Zakeeruddin, S.M.; Moser, J.-E.; Grätzel, M.; et al. Dye-sensitized solar cells for efficient power generation under ambient lighting. *Nat. Photonics* **2017**, *11*, 372–378. [CrossRef]
20. Cao, Y.; Liu, Y.; Zakeeruddin, S.M.; Hagfeldt, A.; Grätzel, M. Direct Contact of Selective Charge Extraction Layers Enables High-Efficiency Molecular Photovoltaics. *Joule* **2018**, *2*, 1108–1117. [CrossRef]
21. Tanaka, E.; Michaels, H.; Freitag, M.; Robertson, N. Synergy of co-sensitizers in a copper bipyridyl redox system for efficient and cost-effective dye-sensitized solar cells in solar and ambient light. *J. Mater. Chem. A* **2020**, *8*, 1279–1287. [CrossRef]
22. Michaels, H.; Rinderle, M.; Freitag, R.; Benesperi, I.; Edvinsson, T.; Socher, R.; Gagliardi, A.; Freitag, M. Dye-sensitized solar cells under ambient light powering machine learning: Towards autonomous smart sensors for the internet of things. *Chem. Sci.* **2020**, *11*, 2895–2906. [CrossRef]
23. Zhang, D.; Stojanovic, M.; Ren, Y.; Cao, Y.; Eickemeyer, F.T.; Socie, E.; Vlachopoulos, N.; Moser, J.-E.; Zakeeruddin, S.M.; Hagfeldt, A.; et al. A molecular photosensitizer achieves a Voc of 1.24 V enabling highly efficient and stable dye-sensitized solar cells with copper(II/I)-based electrolyte. *Nat. Commun.* **2021**, *12*, 1777. [CrossRef] [PubMed]
24. Chatterjee, S.; Webre, W.A.; Patra, S.; Rout, B.; Glass, G.A.; D'Souza, F.; Chatterjee, S. Achievement of superior efficiency of $TiO_2$ nanorod-nanoparticle composite photoanode in dye sensitized solar cell. *J. Alloys Compd.* **2020**, *826*, 154188. [CrossRef]
25. Ding, Y.; Yao, J.; Hu, L.; Dai, S. Controlled synthesis of symbiotic structured $TiO_2$ microspheres to improve the performance of dye-sensitized solar cells. *Sol. Energy* **2019**, *183*, 587–593. [CrossRef]
26. Wan, T.; Ramakrishna, S.; Liu, Y. Recent progress in electrospinning $TiO_2$ nanostructured photo-anode of dye-sensitized solar cells. *J. Appl. Polym. Sci.* **2018**, *135*, 45649. [CrossRef]
27. Xu, Z.; Li, Y.; Li, Y.; Yuan, S.; Hao, L.; Gao, S.; Lu, X. Theoretical study of T shaped phenothiazine/carbazole based organic dyes with naphthalimide as π-spacer for DSSCs. *Spectrochim. Acta Part A Mol. Biomol. Spectrosc.* **2020**, *233*, 118201. [CrossRef]
28. Biancardo, M.; West, K.; Krebs, F.C. Optimizations of large area quasi-solid-state dye-sensitized solar cells. *Sol. Energy Mater. Sol. Cells* **2006**, *90*, 2575–2588. [CrossRef]
29. Biancardo, M.; West, K.; Krebs, F.C. Quasi-solid-state dye-sensitized solar cells: Pt and PEDOT:PSS counter electrodes applied to gel electrolyte assemblies. *J. Photochem. Photobiol. A Chem.* **2007**, *187*, 395–401. [CrossRef]
30. Nurlalela, A.; Yuniarti, E.; Ahmiatri Saptari, S.; Fisika, J.; Aplikasinya, D. Synthesize of $TiO_2$ nanoparticles by planetary ball mill for dye-sensitized solar cells (DSSC) photoelectrode application. *SPEKTRA J. Fis. Dan Apl.* **2023**, *8*, 83–92.
31. Rajeshkanna, S.; Nirmalkumar, O. Synthesis and characterization of Cu nanoparticle using high energy ball milling route and compare with Scherrer Equation. *Int. J. Sci. Eng. Res.* **2014**, *2*, 305.
32. Dawo, C.; Chaturvedi, H. Recent advances in the development of flexible dye-sensitized solar cells: Fabrication, challenges and applications-a review. *Flex. Print. Electron.* **2023**, *8*, 013001. [CrossRef]

33. Ito, S.; Takahashi, K.; Yusa, S.-I.; Imamura, T.; Tanimoto, K. Effects of Homogenization Scheme of TiO$_2$ Screen-Printing Paste for Dye-Sensitized Solar Cells. *Int. J. Photoenergy* **2012**, *2012*, 405642. [CrossRef]

34. Huang, N.; Sebo, B.; Pan, M.M.; Liu, Y.M.; Peng, T.; Sun, W.W.; Bu, C.H.; Zhao, X.Z. A viscous titania paste with a single coating-sintering step for 8–24μm thick, high-haze, high-quality TiO$_2$ films of dye-sensitized solar cells. *Sol. Energy* **2013**, *97*, 266–272. [CrossRef]

35. Hong, C.K.; Ko, H.-S.; Han, E.-M.; Yun, J.-J.; Park, K.-H. Enhanced efficiency of dye-sensitized solar cells doped with green phosphors LaPO4:Ce, Tb or (Mg, Zn)Al$_{11}$O$_{19}$:Eu. *Nanoscale Res. Lett.* **2013**, *8*, 219. [CrossRef] [PubMed]

36. Yasuhiro, Y.; Masahide, K.; Hiroshi, S.; Satoshi, U.; Junya, K.; Fumio, S.; Kazuki, T.; Tsubasa, S.; Seigo, I. 10% Efficiency Dye-sensitized Solar Cells Using P25 TiO2 Nanocrystalline Electrode Prepared by a Bead-milling Method. *Chem. Lett.* **2011**, *40*, 1220–1222. [CrossRef]

37. Mehnane, H.F.; Wang, C.; Kondamareddy, K.K.; Yu, W.; Sun, W.; Liu, H.; Bai, S.; Liu, W.; Guo, S.; Zhao, X.-Z. Hydrothermal synthesis of TiO$_2$ nanoparticles doped with trace amounts of strontium, and their application as working electrodes for dye sensitized solar cells: Tunable electrical properties & enhanced photo-conversion performance. *RSC Adv.* **2017**, *7*, 2358–2364. [CrossRef]

38. Nguyen, H.H.; Gyawali, G.; Kim, T.H.; Bin Humam, S.; Lee, S.W. Blue TiO$_2$ polymorph: An efficient material for dye-sensitized solar cells fabricated using a low-temperature sintering process. *Prog. Nat. Sci. Mater. Int.* **2018**, *28*, 548–553. [CrossRef]

39. Abdullah, N.A.; Ali, B.; Jabbar, H. Study the Effect of TiO$_2$ Nanoparticles in Multilayers of Photoelectrode Prepared by Ball Milling Technique on The Performance of Dye Sensitized Solar Cells (Dsscs). *J. Phys. Conf. Ser.* **2021**, *1818*, 012069. [CrossRef]

40. Ursu, D.; Vajda, M.; Miclau, M. Investigation of the p-type dye-sensitized solar cell based on full Cu$_2$O electrodes. *J. Alloys Compd.* **2019**, *802*, 86–92. [CrossRef]

41. Ursu, D.; Vajda, M.; Miclau, M. Highly efficient dye-sensitized solar cells for wavelength-selective greenhouse: A promising agrivoltaic system. *Int. J. Energy Res.* **2022**, *46*, 18550–18561. [CrossRef]

42. Ursu, D.; Vajda, M.; Mareş, M.C.; Miclau, N.; Miclau, M.; Svasta, P. Exploring the Photo-Electrochemical Processes of the Parallel Connected DSSCs in Indoor Conditions. In Proceedings of the 2023 46th International Spring Seminar on Electronics Technology (ISSE), Timisoara, Romania, 10–14 May 2023; pp. 1–5.

43. Williamson, G.K.; Hall, W.H. X-ray line broadening from filed aluminium and wolfram. *Acta Metall.* **1953**, *1*, 22–31. [CrossRef]

44. Gowthambabu, V.; Deshpande, M.; Govindaraj, R.; Nithesh Krishna, V.K.; Leela Charumathi, M.; Manish Kumar, J.; Dhilip Vignesh, M.S.; Isaac Daniel, R.; Ramasamy, P. Synthesis of anatase TiO$_2$ microspheres and their efficient performance in dye-sensitized solar cell. *J. Mater. Sci. Mater. Electron.* **2021**, *32*, 26306–26317. [CrossRef]

45. Maurya, I.C.; Senapati, S.; Singh, S.; Srivastava, P.; Maiti, P.; Bahadur, L. Effect of Particle Size on the Performance of TiO$_2$ Based Dye-Sensitized Solar Cells. *ChemistrySelect* **2018**, *3*, 9872–9880. [CrossRef]

46. Chougala, L.; Yatnatti, M.; Linganagoudar, R.; Kamble, R.; Kadadevarmath, J. A Simple Approach on Synthesis of TiO$_2$ Nanoparticles and its Application in dye Sensitized Solar Cells. *J. Nano Electron. Phys.* **2017**, *9*, 04005-1. [CrossRef] [PubMed]

47. Mustafa, M.N.; Shafie, S.; Wahid, M.H.; Sulaiman, Y. Preparation of TiO$_2$ compact layer by heat treatment of electrospun TiO$_2$ composite for dye-sensitized solar cells. *Thin Solid Film.* **2020**, *693*, 137699. [CrossRef]

48. Gonçalves, P.; Bertholdo, R.; Dias, J.; Maestrelli, S.; Giraldi, T. Evaluation of the Photocatalytic Potential of TiO$_2$ and ZnO Obtained by Different Wet Chemical Methods. *Mater. Res.* **2017**, *20*, 181–189. [CrossRef]

49. Raskó, J.; Kecskés, T.; Kiss, J. Adsorption and reaction of formaldehyde on TiO$_2$-supported Rh catalysts studied by FTIR and mass spectrometry. *J. Catal.* **2004**, *226*, 183–191. [CrossRef]

50. Nithya, N.; Gopi, S.; Bhoopathi, G. An Amalgam of Mg-Doped TiO$_2$ Nanoparticles Prepared by Sol–Gel Method for Effective Antimicrobial and Photocatalytic Activity. *J. Inorg. Organomet. Polym. Mater.* **2021**, *31*, 4594–4607. [CrossRef]

51. Carneiro, J.O.; Azevedo, S.; Fernandes, F.; Freitas, E.; Pereira, M.; Tavares, C.J.; Lanceros-Méndez, S.; Teixeira, V. Synthesis of iron-doped TiO$_2$ nanoparticles by ball-milling process: The influence of process parameters on the structural, optical, magnetic, and photocatalytic properties. *J. Mater. Sci.* **2014**, *49*, 7476–7488. [CrossRef]

52. Hirose, F.; Kuribayashi, K.; Suzuki, T.; Narita, Y.; Kimura, Y.; Niwano, M. UV Treatment Effect on TiO$_2$ Electrodes in Dye-Sensitized Solar Cells with N719 Sensitizer Investigated by Infrared Absorption Spectroscopy. *Electrochem. Solid-State Lett.* **2008**, *11*, A109. [CrossRef]

53. Sarker, S.; Ahammad, A.J.S.; Seo, H.W.; Kim, D.M. Electrochemical Impedance Spectra of Dye-Sensitized Solar Cells: Fundamentals and Spreadsheet Calculation. *Int. J. Photoenergy* **2014**, *2014*, 851705. [CrossRef]

54. Lei, B.-X.; Luo, Q.-P.; Yu, X.-Y.; Wu, W.-Q.; Su, C.-Y.; Kuang, D.-B. Hierarchical TiO$_2$ flowers built from TiO$_2$ nanotubes for efficient Pt-free based flexible dye-sensitized solar cells. *Phys. Chem. Chem. Phys.* **2012**, *14*, 13175–13179. [CrossRef] [PubMed]